Seasonality of the Energy Transfers in the Azores Current

João H. Bettencourt and C. Guedes Soares

Centre for Marine Technology and Ocean Engineering (CENTEC)
Instituto Superior Técnico, Universidade de Lisboa
Av. Rovisco Pais, 1049-001 Lisboa
Portugal

Corresponding author: C. Guedes Soares (c.guedes.soares@centec.tecnico.ulisboa.pt)

Key Points:

- A climatological simulation of the Eastern Central North Atlantic and the Azores Current is performed
- Azores Current is stable throughout the year due to constant reservoir of available potential energy
- Mean current is maintained by inverse barotropic energy transfers by Reynolds stresses

Abstract

The seasonal variability of the Azores Current energy transfers is studied using the output from a regional ocean model of the Eastern Central North Atlantic, forced by climatological surface fluxes and open ocean boundary conditions. The results show a stable Azores Current with baroclinic energy transfers supporting the current's energetics. Inverse barotropic energy transfers that feed the mean flow are several orders of magnitude smaller but this mechanism is active all year due to the Reynolds Stress convergence. These results support the findings of a stable Azores Current all year round.

Plain Language Summary

The Azores Current is a permanent zonal current in the Eastern North Atlantic that exhibits strong meandering about its mean position. The meanders grow until they detach from the main current, forming mesoscale cyclonic and anticyclonic eddies that travel westward. The cycle of meander formation, growth and dettachment has been so far studied in simplified settings. In our study, we analyze the seasonal cycle of energy transformations in the Azores Current that supports the meandering and eddy formation from a realistic point of view using a climatological simulation of the ocean dynamics in the Eastern North Atlantic. We found that the cycle occurs throughout the year with small seasonal changes. The stability of the cycle is related to the year-round uplifted constant density surfaces that creates a permanent reservoir of potential energy that is transformed in kinetic energy by baroclinic instability.

1 Introduction

The Azores Current (AzC) is a permanent eastward zonal jet located in the northern limit of the subtropical gyre of the North Atlantic, extending from west of the Mid-Atlantic Ridge (Klein & Siedler, 1989; Richardson, 1983) to the vicinity of the African Coast near the Gulf of Cadiz (Martins et al., 2002), where it turns south and joins the subtropical gyre circulation (Brügge, 1995; Klein & Siedler, 1989; Maillard & Käse, 1989)

The AzC has its origin at about 40ºN 45ºW, where the Gulf Stream branches into the northern branch of the North Atlantic Current and the southern branch that feeds the AzC (Brügge, 1995; Klein & Siedler, 1989; Krauss & Käse, 1984). Notwithstanding the AzC source region, modeling studies have found that the AzC owes much of its existence to the beta plume mechanism due to the mixing of the light North Atlantic Central Water with the underlying heavy Mediterranean Outflow Water in the Gulf of Cadiz (Jia, 2000; Kida et al., 2008; Özgökmen et al., 2001; A. Peliz et al., 2007). The AzC jet lies south of the Azores Archipelago between 32º and 36º N (Brügge, 1995; Klein & Siedler, 1989; Stramma & Müller, 1989) and transports circa 10 Sv (1 Sv = 10^6 m3/s) in the top 800 m at 35º-33º W with surface velocities above 10 cm/s (Klein & Siedler, 1989; Stramma & Müller, 1989). Transport and velocities in the AzC decrease eastward, as observed by Stramma and Müller (1989), who found 8 Sv (0 - 800 m) and surface speeds below 9 cm/s at 26º 30'W. The vertical structure of the AzC can penetrate to 2000 m (Alves & Verdière, 1999; Gould, 1985) with an e-folding depth of 600 m (Käse et al., 1985) and with transports concentrated in the upper water column (40% of transport at 33ºW above 200 m), (Klein & Siedler, 1989). The AzC is a permanent feature of the circulation in the Eastern North Atlantic but displays clear, albeit small, seasonal changes in position and strength. In its western part, the AzC is connected to the source region by a quasi-uniform current in the winter, that branches in two in the summer, with the southern branch performing a cyclonic meander (Klein & Siedler, 1989). In

the winter, the AzC is displaced to the north of the thermal front while in the summer the current axis is displaced to the south (Stramma & Müller, 1989; Stramma & Siedler, 1988). The structure of the surface circulation shows enhanced meandering and southward branching in the winter (Martins et al., 2002; Traon & Mey, 1994) while the AzC transports increase suddenly and the current deepens from winter to spring (Alves & Verdière, 1999)

The AzC is marked by strong meandering and pinching off of mesoscale eddies (Gould, 1985). The typical meander length scale is 200 - 400 km with an eastward phase speed of roughly 1.5 km day^{-1} and time scales of 20 - 120 days (Maillard & Käse, 1989; Traon & Mey, 1994). Cold-core cyclonic (CC) eddies form as far east as 25º W as plumes of northern cold water and propagate westward at 2-3 km day^{-1}, increasing their intensity (Gould, 1985; Pingree et al., 1999). The mechanism of eddy formation in the AzC forms CC cold-core eddies to the south of the AzC axis and warm-core anticyclonic (AC) eddies to the north, by the nonlinear growth of meander amplitude that eventually causes the wavy form to break into isolated, closed, rotating features with a definite relative vorticity sign, enclosed in waters with ambient vorticity of opposite sign (Alves et al., 2002). Thus, a CC eddy is formed when a meander grows southward creating a plume of cold water south of the current axis, and breaks; an AC eddy forms when a meander grows northward, bringing warm water plume north of the current axis, and breaks. Analysis of altimetry and drifter records of Aguiar et al. (2011) shows that CCs are more numerous than ACs and that they form at a faster rate (1.4 – 2.4 year-1 vs. 1.2-1.7 year-1).

Meander growth and eddy detachment in the AzC is the result of the baroclinic instability of the AzC jet (Alves & Verdière, 1999; Kielmann & Käse, 1987), as a baroclinically unstable eastward flowing jet will grow sufficiently large meanders for eddy detachment to occur as potential vorticity conservation implies large changes in relative vorticity along the path of a fluid element (Ikeda, 1981). Meander growth rates and phase speeds decrease with an increasing amplitude as nonlinearity and dissipation arrest the meander growth (Kielmann & Käse, 1987; Orlanski & Cox, 1972; Wood, 1988).

The analysis of the energetics of ocean currents has been fruitful in explaining the mesoscale structure of the currents and their evolution. Early numerical and field studies of the Gulf Stream, e.g. Orlanski and Cox (1972), Rossby (1987), showed the importance of the baroclinic energy transfer in initiating and sustaining the mesoscale meander and eddy fields. In the Gulf Stream region, mean available potential energy (MAPE) is the major energy reservoir (Kang & Curchitser, 2015), and the main energy transfers are barotropic, from mean to eddy kinetic energy directly (MKE $\rightarrow$ EKE) and from MKE to EKE via MAPE and eddy available potential energy (MKE $\rightarrow$ MAPE $\rightarrow$ EAPE $\rightarrow$ EKE), through Ekman pumping (Kang & Curchitser, 2015).

In the open North Atlantic Ocean, the situation is different: although the main energy reservoir is still MAPE, the main eddy energy supply path is a baroclinic transfer from EAPE to EKE, and an inverse barotropic transfer from EKE to MKE can be observed (Beckmann et al., 1994). Incidentally, the same configuration of energy transfers is also found for the Gulf Stream in the open ocean (Kang & Curchitser, 2015). For the AzC, idealized model studies have unveiled an energy cycle in general agreement with the open ocean results of Beckmann et al (1994): EKE fed mainly by baroclinic energy transfer and an inverse barotropic transfer by which the eddy field sustains the mean flow (Alves & Verdière, 1999; Kielmann & Käse, 1987).

In these primitive equation model studies instabilities are triggered in a baroclinically unstable zonal base flow (Alves & Verdière, 1999), and in a first phase an increase of EKE at the expense of EAPE occurs. In this phase, peaks in EKE coincide with the detachment of AC eddies. A second phase ensues where strong Reynolds stress convergence feed the main flow (MKE) at the expense of EKE; MKE is maximum half-way in the second phase (Alves & Verdière, 1999). Superimposed on this cycle is a weak and intermittent barotropic energy transfer from MKE to EKE due to the shear instability of the generated mean flow (Alves & Verdière, 1999; Wood, 1988). The energy cycle has time scales of ~200 days, but without restoration of the MAPE reservoir only the first cycle will occur and the instabilities will dye-off (Alves & Verdière, 1999).

Although the energetics cycle of the AzC is relatively well established, some questions remain regarding its seasonality and recurrence with time. Does the cycle occur all year round? Are there any reversals in the energy flows during the year in response to seasonal variations of, say, atmospheric forcing, or density stratifications? In this paper, we try to answer these questions using a primitive equation simulation of the AzC in the regional setting of the Eastern Central North Atlantic. In section 2 the numerical model and the simulation setup are described; in section 3 the results of the simulation are presented and an analysis of the AzC energetics is made. Section 4 concludes the paper.

2 Materials and Methods

2.1 Circulation model

The model used in this work is the Regional Ocean Modelling System (ROMS, (Shchepetkin & McWilliams, 2003, 2005). ROMS is a free-surface terrain-following model that solves the primitive equations using the Boussinesq and hydrostatic approximations. In the primitive equation framework, of the 3d velocity $\vec{U} = (u, v, w)$ only the zonal and meridional velocity components (u,v) belong to the prognostic variables set, the other member being the free surface elevation ζ. The momentum equations in Cartesian coordinates are (Haidvogel et al., 2008):

$$\frac{\partial(H_z u)}{\partial t} + \frac{\partial(uH_z u)}{\partial x} + \frac{\partial(vH_z u)}{\partial y} + \frac{\partial(\Omega H_z u)}{\partial s} - fH_z v = -\frac{H_z}{\rho_0}\frac{\partial p}{\partial x} - H_z g\frac{\partial \zeta}{\partial x} - \frac{\partial}{\partial s}\left(\overline{u'w'} - \frac{v}{H_z}\frac{\partial u}{\partial s}\right), \quad (1)$$

$$\frac{\partial(H_z v)}{\partial t} + \frac{\partial(uH_z v)}{\partial x} + \frac{\partial(vH_z v)}{\partial y} + \frac{\partial(\Omega H_z v)}{\partial s} + fH_z u = -\frac{H_z}{\rho_0}\frac{\partial p}{\partial y} - H_z g\frac{\partial \zeta}{\partial y} - \frac{\partial}{\partial s}\left(\overline{v'w'} - \frac{v}{H_z}\frac{\partial v}{\partial s}\right), \quad (2)$$

$$0 = -\frac{1}{\rho_0}\frac{\partial p}{\partial s} - \frac{g}{\rho_0}H_z\rho, \quad (3)$$

where (3) is the vertical momentum equation, which in the hydrostatic approximation is a simple relationship between the vertical pressure gradient and the weight of the fluid column. The continuity equation is:

$$\frac{\partial \zeta}{\partial t} + \frac{\partial(H_z u)}{\partial x} + \frac{\partial(H_z v)}{\partial y} + \frac{\partial(H_z \Omega)}{\partial s} = 0, \quad (4)$$

and the scalar transport equation is:

$$\frac{\partial(H_z C)}{\partial t} + \frac{\partial(uH_z C)}{\partial x} + \frac{\partial(vH_z C)}{\partial y} + \frac{\partial(\Omega H_z C)}{\partial s} = -\frac{\partial}{\partial s}\left(\overline{c'w'} - \frac{v}{H_z}\frac{\partial C}{\partial s}\right) + C_{source}. \quad (5)$$

In (1-5), s is a vertical stretched coordinate that varies from $s=-1$ (bottom) to $s=0$ (surface). The vertical grid stretching parameter is $H_z = \partial z/\partial s$ and Ω is the vertical velocity in the s coordinate. The Coriolis parameter is f, p is the hydrostatic pressure and g is the acceleration of gravity. An overbar denotes averaged quantities, primed (′) variables are departures from the average and ν is molecular diffusivity (momentum or scalar). Vertical turbulent momentum and tracer fluxes are:

$$\overline{u'w'}=K_M\frac{\partial u}{\partial z};\ \overline{v'w'}=-K_M\frac{\partial v}{\partial z};\ \overline{c'w'}=-K_H\frac{\partial \rho}{\partial z}, \quad (6)$$

where K_M and K_H are momentum and tracer eddy diffusivities. The equation of state for seawater is given by $\rho=f(C,p)$. C_{source} is the tracer source/sink term.

ROMS is highly configurable for realistic applications and has been applied to a wide variety of space and time scales across the globe (Haidvogel et al., 2008).

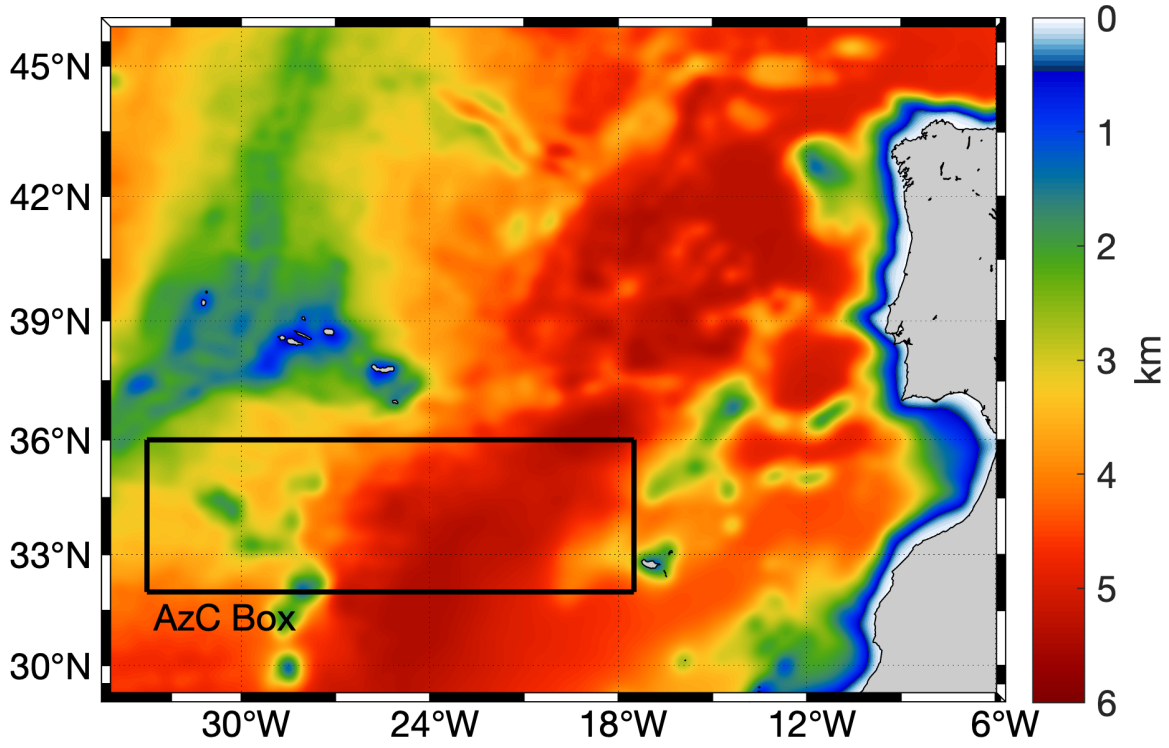

Figure 1. Domain of the ROMS simulation. The AzC box is the region used in the analysis of the AzC energy transfers. Box limits are 33º to 17.5ºW and 32º to 36º N.

The model domain (Figure 1) is part of the Eastern Central North Atlantic and covers the western Iberian margin extending to the Azores and Madeira archipelagos (34.4º to 5.7ºW and 29º to 46ºN). The average horizontal resolution is 4.2 km in the meridional direction and 4.4 km in the zonal direction. The vertical discretization used 20 sigma layers, stretched to increase the resolution near the surface and bottom. The bathymetry is interpolated from ETOPO and smoothed to satisfy a topographic stiffness-ratio of 0.2 (Haidvogel & Beckmann, 1999). The minimum depth used is 10 m.

The model configuration uses a third-order upstream advection scheme for momentum and tracers, a fourth-order centred scheme for vertical advection of momentum and tracers, and the KPP scheme for vertical mixing (Large et al., 1994). Explicit horizontal momentum and tracer diffusion is set to zero. Bottom drag uses a quadratic law with drag coefficient of 0.003.

The model is run in climatological mode where a yearly cycle is repeated for 20 years. The model is forced by surface monthly climatological momentum, heat, freshwater and shortwave radiation fluxes from the Comprehensive Ocean-Atmosphere Data Set (Woodruff et al., 1998), that collects global weather observations taken near the ocean's surface since 1854, primarily from merchant ships. At the open boundaries, values of 2D (barotropic) and 3D (baroclinic) velocities, and active tracers (potential temperature and salinity) are nudged to climatological values. The offline nesting procedure employed here uses a nudging region of 40 km along the model boundaries. In this layer, the 3-D model variables (temperature, salinity, and currents) are pushed toward their climatological values. The nudging time scale is set to 5 days at the boundaries, decaying linearly to zero inside the nudging layer. At the boundaries, outgoing radiation conditions are used for the baroclinic variables (Marchesiello et al., 2001). Climatological sea surface height and barotropic currents were imposed at the boundaries using Chapman boundary conditions (Chapman, 1985).

2.2 Energetics formalism

In this work the formalism[1] of Kang and Curchitser(2015) is used to analyze the energetics of the AzC. The total density is $\rho(x,y,z,t) = \rho_r(z) + \rho_a(x,y,z,t)$ where $\rho_r(z)$ is the reference density and ρ_a is the perturbation density. The reference density is defined as the density of an globally static, stably stratified state of the ocean, obtained from its actual state by an adiabatic rearrangement of the fluid, conserving salt and mass (Lorenz, 1955; Saenz et al., 2015). The choice of $\rho_r(z)$ fell on the global reference stratification obtained by Saenz et al. (2015) from the annually averaged temperature and salinity fields of the World Ocean Atlas 2009. Arguably, this choice is consistent with the definition of $\rho_r(z)$ as a global state of rest; choosing a local $\rho_r(z)$, as is more usual (Kang & Curchitser, 2015) would imply that there exist horizontal reference density gradients, in contradiction to the definition of the reference density. The pressure is $p = p_r + p_a$, where p_r is the pressure associated to ρ_r by the hidrostatic relation and p_a the perturbation pressure associated with the perturbation density ρ_a by the same relation. The density transport equation is thus

$$\frac{\partial \rho_a}{\partial t} + \vec{U}_H \cdot \nabla \rho_a = \frac{\rho_0}{g} N^2 w + F_p + D_p, \qquad (7)$$

where $\vec{U}_H = (u, v)$ and N^2 is the buoyancy frequency:

$$N^2 = \frac{g}{\rho_0} \frac{d\rho_r}{dz}.$$

and Fp and Dp are buoyancy forcing and dissipation, respectively. The mean and perturbation (or eddy) energy equations are obtained by decomposing the relevant fields into its mean and fluctuating parts. Here, the mean is taken as the zonal average of the field in the AzC box:

[1] The formalism is here introduced in a implementation-independent notation. The actual expressions used in the calculations are adapted to the ROMS curvilinear fractional coordinate system.

$$\overline{(\quad)} = \frac{1}{L}\int_0^L (\quad)\, dx,$$

where L is the length of the AzC box. This choice is consistent with earlier studies of the energetics of the AzC, e.g Alves and Verdière (1999), and is chosen over, say a temporal mean, because of the stable zonal character of the mean AzC and because, in the presence of strong meandering, time fluctuations are more a result of the meandering itself than of time fluctuations (Rossby, 1987). The total field ϕ is then the sum of its mean part $\bar{\phi}$ and its fluctuating part ϕ'. For density it is $\bar{\rho} = \rho_r + \overline{\rho_a}$ and $\rho' = \rho'_a$. The horizontal kinetic energy density (KE, energy per unit volume) is decomposed in mean (MKE) and fluctuating (EKE) parts:

$$\text{KE=MKE+EKE=}\frac{1}{2}\rho_0(\bar{u}^2 + \bar{v}^2) + \frac{1}{2}\rho_0\left(\overline{u'^2 + v'^2}\right). \tag{8}$$

The available potential energy (APE) is computed with the linear expression of Gill (1982):

$$\text{APE=}\frac{g^2\rho_a^2}{2\rho_0 N^2},$$

that is the leading term of the Taylor series expansion of the exact APE expression (Kang & Fringer, 2010). The consequences of this choice of PE formulation are considered in section 4. The APE density is also decomposed in mean (MAPE) and fluctuating (EAPE) parts:

$$\text{APE=MAPE+EAPE=}\frac{g^2\bar{\rho}_a^2}{2\rho_0 N^2} + \frac{g^2\overline{\rho'^2_a}}{2\rho_0 N^2}. \tag{9}$$

The equation for MKE is obtained multiplying the momentum equations (1) and (2) by $\rho_0\bar{u}$ and $\rho_0\bar{v}$ respectively, and averaging their sum:

$$\frac{\partial MKE}{\partial t} + \nabla\cdot\left(\overline{\vec{U}_H}MKE\right) + \nabla\cdot\left(\overline{\vec{U}_H}\overline{p_a}\right) = -g\overline{\rho_a}\overline{w} - \rho_0\left[\bar{u}\nabla\cdot\left(\overline{\vec{U}'u'}\right) + \bar{v}\nabla\cdot\left(\overline{\vec{U}'v'}\right)\right] + \overline{\vec{\vec{U}}}\cdot\overline{\vec{F}} + \overline{\vec{\vec{U}}}\cdot\overline{\vec{D}}. \tag{10}$$

The 2nd (cv_0) and 3rd terms of the left-hand side (lhs) of (10) represent the divergence of the MKE flux into the domain. The first term of the right-hand side (rhs), cm_0, is the acceleration of the mean flow due to mean buoyancy work; the second term, ck_0, is the Reynolds stress work that transfers energy from the eddy to the mean flow. The third and fourth terms are the MKE forcing by mean surface fluxes $\overline{\vec{F}}$and the dissipation of MKE by mean viscous work $\overline{\vec{D}}$.

The EKE is obtained in a similar fashion by multiplying the momentum equations (1) and (2) by $\rho_0 u'$ and $\rho_0 v'$ and averaging their sum:

$$\frac{\partial EKE}{\partial t} + \nabla\cdot\left(\overline{\vec{U}_H EKE}\right) + \nabla\cdot\left(\overline{\vec{U}'_H p'}\right) = -g\overline{\rho'_a w'} - \rho_0\left[\overline{u'\vec{U}'}\cdot\nabla\bar{u} + \overline{v'\vec{U}'}\cdot\nabla\bar{v}\right] + \overline{\vec{U}'\cdot\vec{F}'} + \overline{\vec{U}'\cdot\vec{D}'}. \tag{11}$$

The 2nd (cv) and 3rd term (cp) of the lhs of (11) are analogous to those of the MKE equation (10). The first and second terms, cm and ck, of the rhs represent EKE production by baroclinic and

barotropic instabilities. The last two terms are the mean forcing of EKE by fluctuating wind stress and mean dissipation of EKE by fluctuating viscous work.

The equations for MAPE and EAPE are obtained by multiplying the density equation (7) by $\frac{g^2\overline{\rho_a}}{2\rho_0 N^2}$ and $\frac{g^2\rho'_a}{2\rho_0 N^2}$ respectively, and averaging the result. The MAPE equation is:

$$\frac{\partial MAPE}{\partial t} + \nabla\cdot\left(\overline{\vec{U}_H} MAPE\right) = g\overline{\rho_a}\overline{w} - \frac{g^2\overline{\rho_a}}{2\rho_0 N^2}\nabla\cdot\left(\overline{\overrightarrow{U'}\rho'_a}\right) + \frac{g^2\overline{\rho_a}}{2\rho_0 N^2}(\overline{F}_r + \overline{D}_r). \quad (12)$$

The second term of the lhs of (12), gv_0, is the flux divergence of MAPE. The first term of the rhs of (12) is $-cm_0$ and the second term, $gp0$, is the EAPE → MAPE energy transfer. The last two terms are the forcing and dissipation of MAPE. The EAPE equation is:

$$\frac{\partial EAPE}{\partial t} + \nabla\cdot\left(\overline{\vec{U}_H EAPE}\right) = g\overline{\rho'_a w'} - \frac{g^2}{2\rho_0 N^2}\overline{\overrightarrow{U'}\rho'_a}\cdot\nabla(\overline{\rho_a}) +$$

$$\frac{g^2}{2\rho_0 N^2}\left(\overline{\rho'_a F'_r} + \overline{\rho'_a D'_r}\right), \quad (13)$$

where the first term of the rhs of (13) is $-cm$ and the second term, gp, is the MAPE→EAPE energy transfer. The last terms are the forcing and dissipation of EAPE. The gp_0 and gp terms exchange energy between MAPE and EAPE due to the action of fluctuating density fluxes. As pointed out in Kang and Curchitser (2015), the terms in the EAPE and MAPE equations depend on the choice of $\rho_r(z)$, except for cm. The sensitivity of this dependence was examined by Kang and Curchitser (2015) that found that it mostly affects MAPE, while the cm_0, gp_0 and gp are only slightly affected by the choice of $\rho_r(z)$.

3 Results

3.1 Circulation

The model achieved equilibrium after a spin up period of 4 model years, after which the volume average total kinetic energy density $1/V\cdot\int_V 0.5\rho(u^2+v^2)\,dV$ (Figure 2a) reaches a plateau and then fluctuates around 1.2 kg m^{-1} s^{-2} until the end of the simulation. Domain averaged temperature levels (Figure 2b) show a strong seasonal signal, superposed to a declining trend from year 4 onward. Domain averaged salinity (Figure 2c) shows a declining trend without clear seasonality.

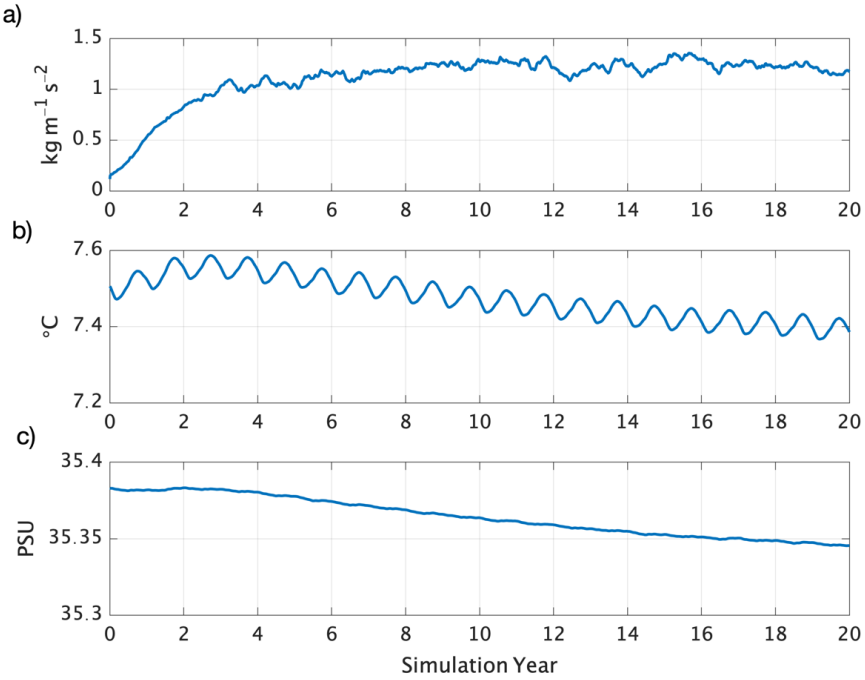

Figure 2. Time series of domain averaged a) kinetic energy density; b) temperature; c) salinity. PSU is Practical Salinity Units.

The average surface velocity field from the ROMS simulation (Figure 3a) shows the characteristic surface circulation patterns in the region. North of 36ºN the circulation is mainly south-eastward due to the southward branches of the Gulf Current that separate approximately at 54ºW, leaving the North Atlantic Drift and the southward PC between 18º and 12ºW (Reverdin et al., 2003). East of the PC the circulation is influenced by the MO and the WIbUS. The main features of the average coastal circulation in the western Iberian shelf are the Cape São Vicente westward jet that flows along the slope of Gulf of Cadiz and the western Iberia coastal counter-flows. The poleward flow along the Iberian margin matches descriptions of the Portugal Coastal Counter-Current, that is known to bend anticyclonically when passing the north-western corner of the Iberian peninsula (Álvarez-Salgado et al., 2003), and of other coastal poleward counter-flows reported in the literature (Peliz et al., 2002, 2005).

Below 36ºN, the AzC appears as the eastward jet between 33º and 36º N, clearly visible in Figure 3a until the Gulf of Cadiz, with maximum velocities of the order of 10 cm s^{-1}. The AzC partially turns south and joins the general westward and southward drift of the West Africa and the subtropical gyre. The eastward jet's location agrees with the well-known AzC location, and it can be seen reaching the Gulf of Cadiz.

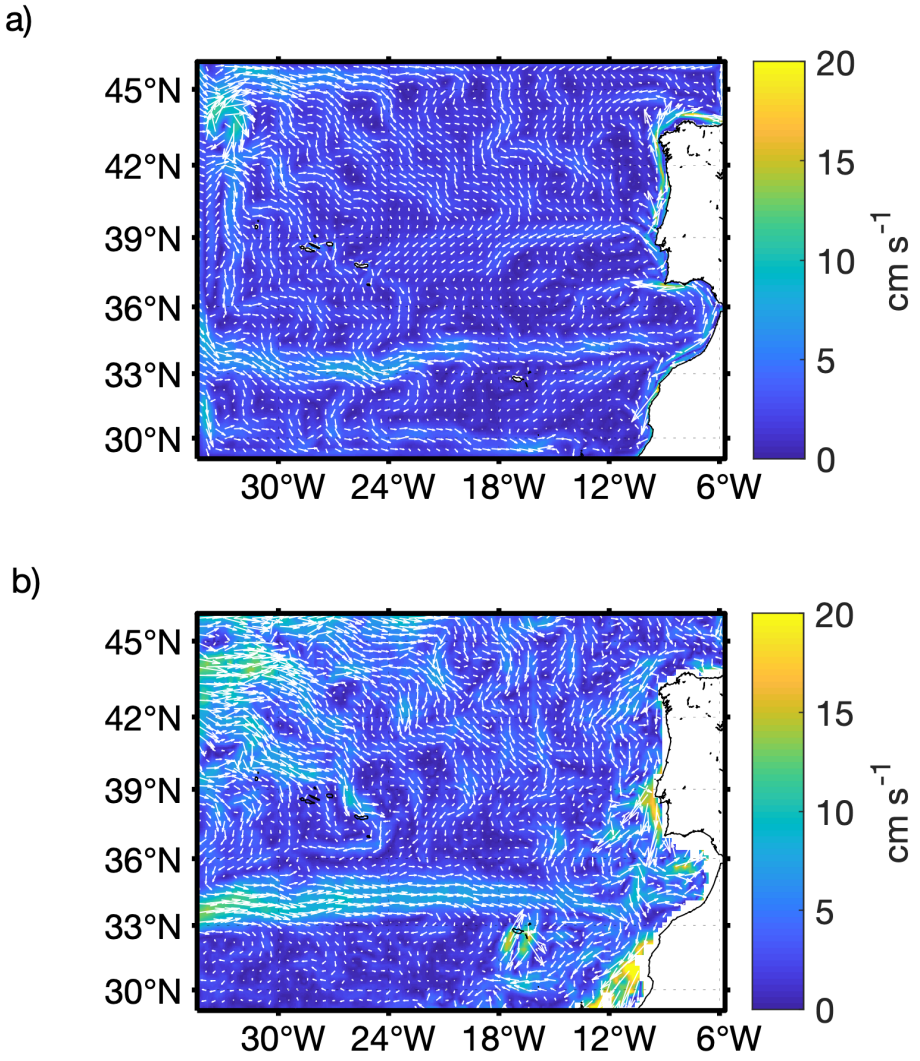

277

278 **Figure 3**. Mean surface horizontal velocity field. a) ROMS simulations; b) SVP climatology.

279 The comparison of the model average surface velocity field with the Surface Velocity
280 Program climatology (Laurindo et al., 2017) (Figure 3b) shows that the model velocities are
281 generally lower than those of the SVP climatology. However, the position of the main features is
282 well reproduced, especially the position of the AzC and the general south-eastward velocity field
283 in the northern part of the domain. The discrepancies highlight the limitations of the limited area
284 modelling approach and the use of a climatological forcing. The first factor introduces errors at
285 the boundaries e.g, the velocity imposed on the boundary is computed from geostrophy only while
286 the SVP dataset is computed from real drifter velocities. The climatological forcing on the other
287 hand limits the model response only to an annual cycle while the SVP dataset contains also
288 interannual forcing effects.

3.2 The Azores Current

The average surface velocity field (Figure 3a) shows the AzC as a quasi-zonal eastward jet. However, the instantaneous velocity field for 4 of March of simulation year (S.Y.) 18 (Figure 4a) shows the AzC, the predominant circulation feature in the region, as a strongly meandering jet with instantaneous velocities up to 50 cm/s in the current axis. The axis itself is severely deformed, forming a cyclonic meander centred at approximately 32ºW. South of the current axis three closed cyclonic circulations can be observed between the western boundary and 30ºW. These cyclones have length scales on the order of 100 – 300 km and are present due to the pinching off of cyclonic vortices formed northward of the jet axis (Alves et al., 2002). In a purely zonal jet, positive (cyclonic) vorticity is found northward of the jet axis and negative (anticyclonic) vorticity is found south of the jet axis.

Although the idealization is far from being verified in this simulation, the situation depicted in Figure 4a conforms to this model. Indeed, just under the meander a weak anticyclonic circulation is found. The stirring (Abraham & Bowen, 2002) of the sea surface temperature (SST) field by the mesoscale circulation is visible in the SST map for 4 March S.Y. 18 (Figure 4b), superposed on the gyre scale SST North-South gradient. The association of the AzC with the SST front is clearly observed as the position of the AzC meander coincides with the position of a strong change in SST. Additionally, the position of the large cyclone south of the current axis matches the position of a pool of cooler water, indicating that the cyclone had its origin north of the current axis and, as it moved south, carried with it the colder waters found north of the jet axis. The seasonality of the AzC is pictured in Figure 5. The winter average AzC core is displaced north of the thermal front (18º C isotherm, Figure 5, panel a), while in the Summer a well-developd seasonal thermocline appears (Figure 5, panel c) The AzC is appears as a surface intensified deep jet, with the Azores Counter-Current flowing northward of the AzC jet, centred at 600 m depth. From Spring (Figure 5 panel b) through Summer (Figure 5 panel c) we observe the broadning and weakening of the average AzC core. In the Autumn (Figure 5 panel d), the AzC starts to strengthen and deepening again. As could be expected from the permanence of the AzC the annual variation of meander size is limited (Figure 6), showing an increase from Winter to Spring and a decrease from Summer to Autumn and Winter.

3.3 Seasonal energy budgets in the AzC

Seasonal energy reservoirs and internal energy transfers are shown in Figure 7. The energy reservoirs are fairly constant during the whole year, in agreement with previous observations of the seasonality of the AzC. The largest reservoir is by far MAPE, followed by EAPE. The fact that the AzC lies in the northern limit of the subtropical gyre, in the frontal region that separates warm subtropical from cold subpolar mode waters guarantees the existence of uplifted isopycnals throughout the year (Pingree et al., 1999; Volkov & Fu, 2011), providing thereby a permanent displacement of the constant density surfaces with respect to the reference state $\rho_r(z)$ and therefore a constant reservoir of APE. The average stratification in the AzC box for each season (winter: DJF; spring: MAM; summer: JJA; autumn: SON) are always less stable than $\rho_r(z)$ (Figure 8) so there is a permanent pool of APE available for conversion. It should be noted that APE reservoir is fed by the atmospheric forcing of the mean currents, through Ekman dynamics, hence it should be interpreted as a representation of the energy input in to the ocean from the atmospheric circulation. EAPE is the second largest energy reservoir and is larger in spring, after being supplied during winter by the APE reservoir at the largest seasonal transfer rate (~81 MW).

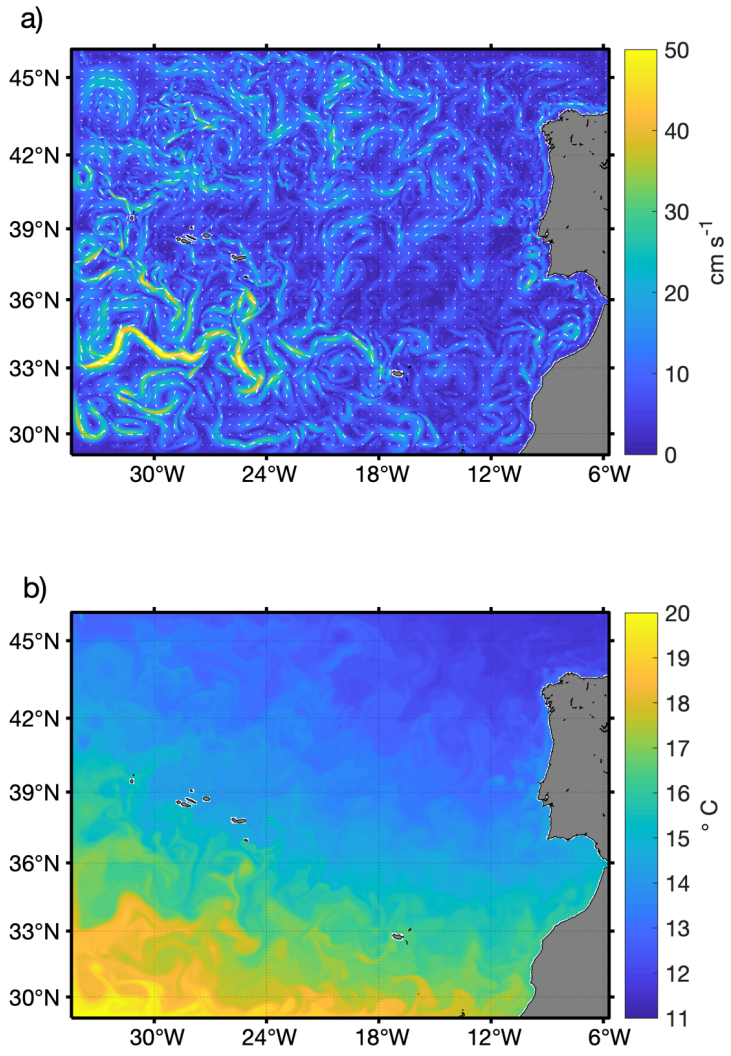

Figure 4. Velocity and temperature surface fields. a) Surface horizontal velocity field for the 4 March S.Y.18; b) Sea Surface Temperature map for the same day.

During Spring, the EAPE reservoir is nearly in balance between the APE input (+17.6 MW) and baroclinic energy flow to EKE (-19.2 MW), with weak net decrease of 1.3 MW. EAPE increases from winter to spring and decresases from spring through autumn, although the summer net energy transfer to EAPE due to fluctuating density fluxes and baroclinicity is positive. Therefore, other energy transfers must account for the decrease in EAPE during summer. The APE reservoir seasonality shows that it attains its increases from autumn through winter to spring and decreases through summer and autumn (Figure 7).

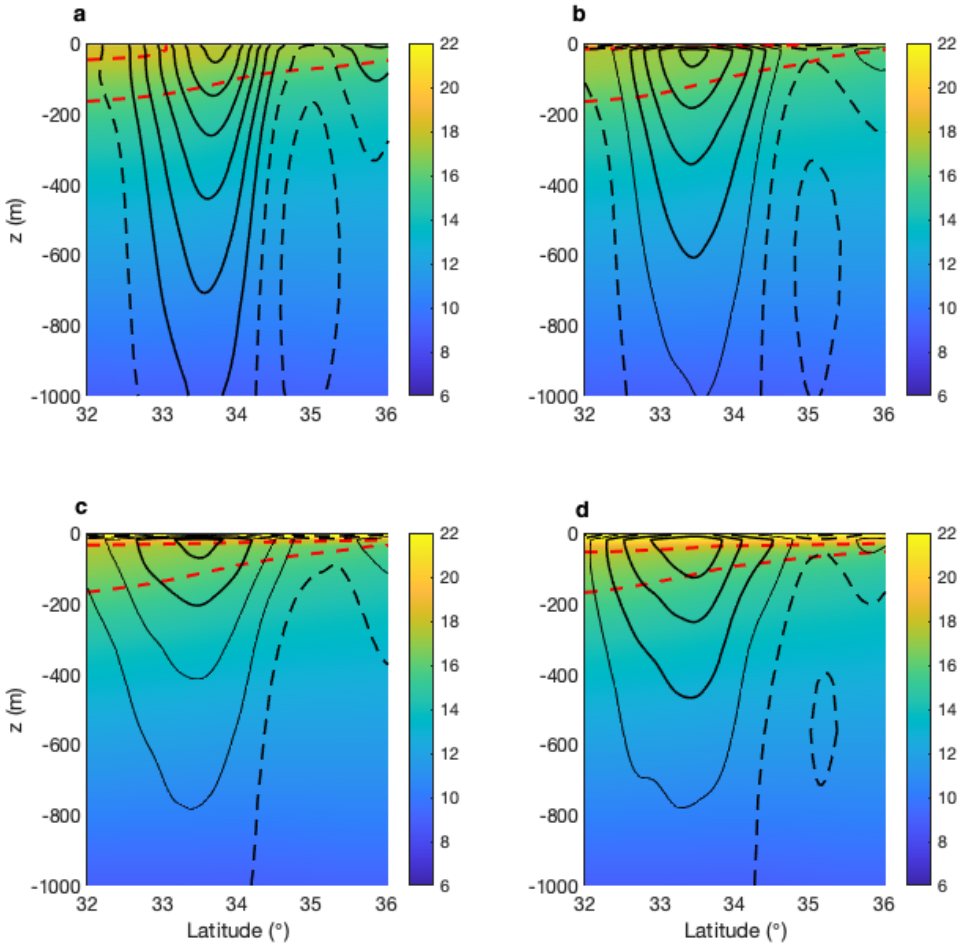

Figure 5. Seasonal average temperature (colormap) and eastward velocity (contours) in the AzC box. a) Winter (DJF); b) Spring (MAM); c) Summer (JJA); d) Autumn (SON). Full contours: u> 0 m/s at 1 cm/s interval; Dashed contours: u<0 m/s at 1 cm/s intervals. Red dashed lines: 16º C and 18ºC isotherms.

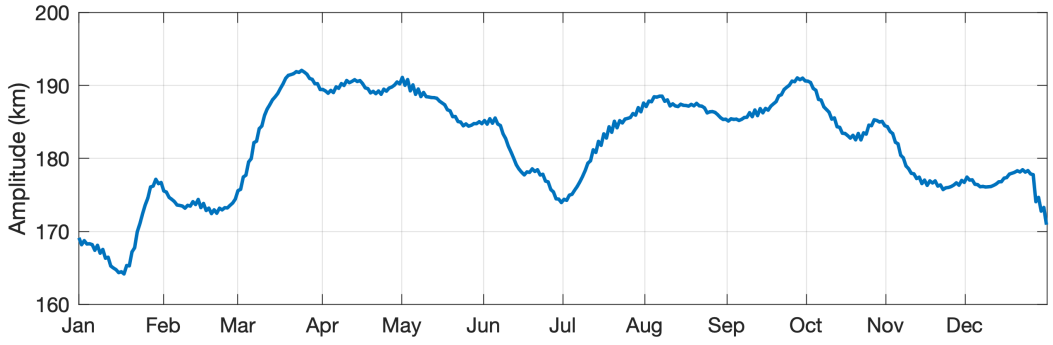

Figure 6. Annual cycle of meander length scale in the AzC. Meander length scale computed as the zonally average distance between positive (northward) and negative (southward) AzC core excursions from the mean AzC core position.

EKE is lowest during winter and increases through Spring, Summer until its maximum in autumn. The yearly change in EKE is 8.3 GJ with a sharp decrease from autumn to winter.Baroclinic energy transfers are always two orders of magnitude larger than the inverse barotropic transfer from EKE to MKE.

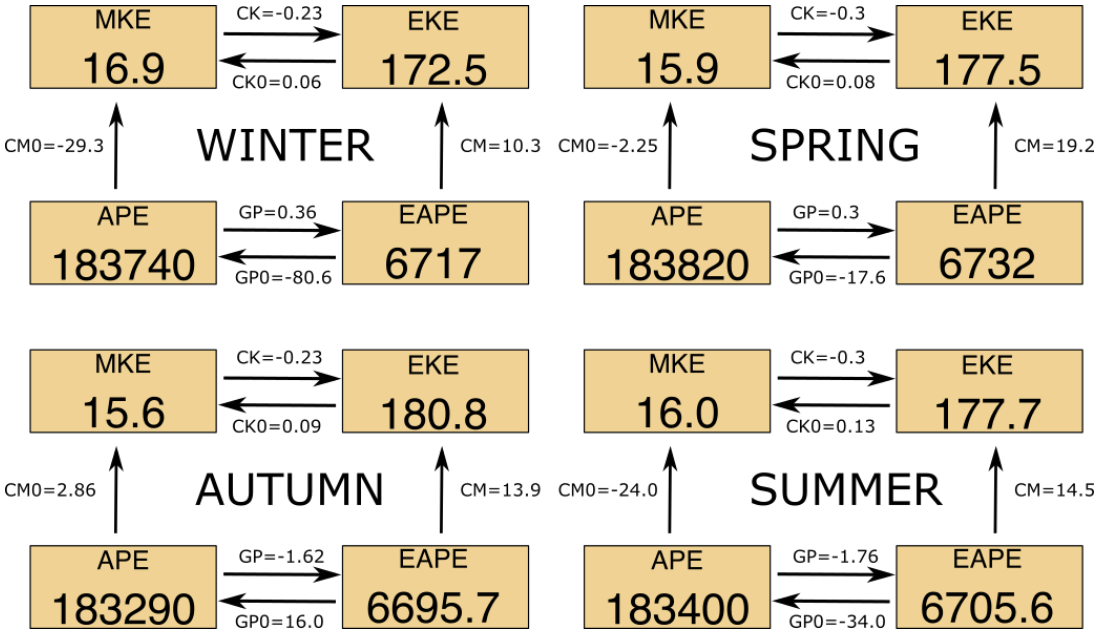

Figure 7. Seasonal mean energy reservoirs and internal transfers. Winter: top left block diagram; Spring: top right block diagram; Summer: bottom right block diagram; Autumn: bottom left block diagram. MKE: Mean Kinetic Energy; EKE: Eddy Kinetic Energy; EAPE: Eddy Available Kinetic Energy; APE: Available Potential Energy. CM(0): baroclinic (eddy) energy transfer; CK(0) is barotropic (eddy) energy transfer. GP(0): potential (eddy) energy transfer. Energy reservoirs are in units of GJ (10^9 Joules) and energy transfers in MW (10^6 Watts). Arrows indicate the direction of the net energy transfers. Values are seasonal mean per unit zonal length. The seasonal means were computed from the 16-year time series of zonal means.

The energy cycle EAPE → EKE → MKE identified in early idealized studies (Alves & Verdière, 1999; Kielmann & Käse, 1987; Wood, 1988) of the AzC is active during the whole year, is strongest in spring (net 19.6 MW) and weakest in winter (net 10.6 MW) and so the results show that throughout the year the mean AzC is fed by the mesoscale circulation. The smallest reservoir is MKE, approximately one order of magnitude smaller than EKE, in agreement with observations of the AzC (Brügge, 1995; Martins et al., 2002) that show that the current's kinetic energy is in large part dominated by eddies. In terms of seasonal means, MKE is continuously supplied by inverse barotropic energy transfers from EKE that are stronger in the summer (0.43 MW) and weaker in the winter (0.29 MW). There is a strong internal energy transfer from MKE to APE in the winter and summer due to Ekmann pumping (Kang & Curchitser, 2015; Volkov & Fu, 2010).

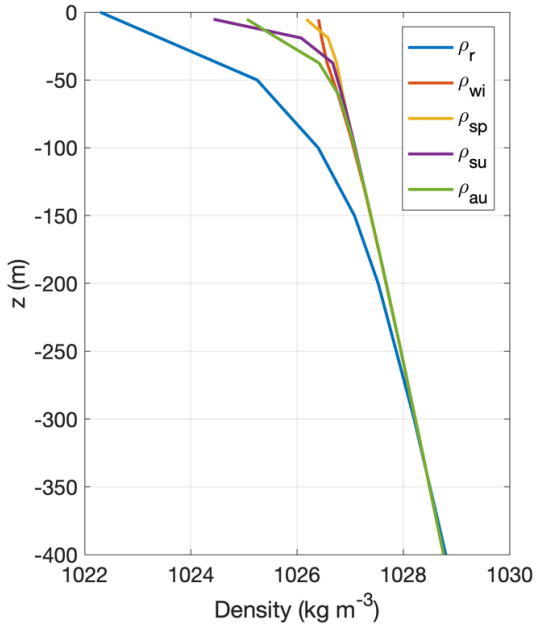

377

378 **Figure 8**. Reference and seasonal stratification profiles averaged in the AzC box. Reference stratification:
379 ρ_r; Winter stratification: ρ_{wi}; Spring stratification: ρ_{sp}; Summer stratification: ρ_{su}; Autumn stratification:
380 ρ_{au}. APE is proportional to the area between the reference and the seasonal stratifications

381 3.4 Seasonal energy transfer cycles

382 The weekly averaged annual cycle of MKE density transfer terms is shown in Figure 9,
383 where the different terms were scaled to fit a common range. The atmospheric forcing ca_0 follows
384 an annual cycle where it is maximum in late winter and minimum in summer.

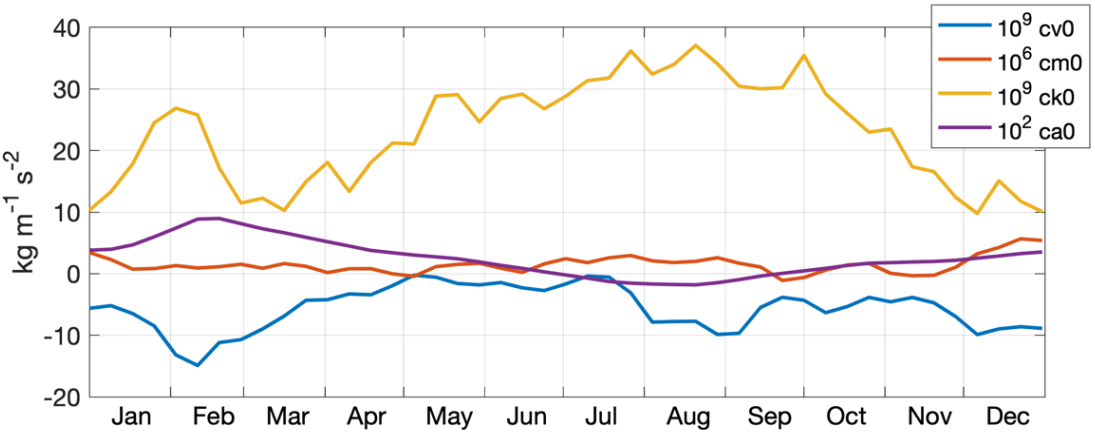

385

386 **Figure 9**. Annual cycle of volume averaged MKE transfer terms. Cv_0: advective flux of MKE; cm_0:
387 Mean buoyancy work; ck_0: Reynolds stress (barotropic) work; ca_0: wind stress work. All terms were
388 scaled to fit the same range. Scaling factors are shown next to the color key. Terms with larger scaling
389 factors are smaller than terms with smaller scaling factors.

390 The variation of the atmospheric forcing in the AzC is largely due to the motion of the large scale
391 atmospheric systems: from January to July in the AzC region the winds change from westerlies to

trades (Hellerman and Rosenstein, 1983). Since $\bar{u}$ of the surface AzC core jet is always positive (Fig 8, left panels), the zonal mean wind power input will change from positive in winter to negative in summer as the zonal wind stress component (Fig 9, top panel). The AzC's $\bar{v}$ at the surface is always negative which, combined with negative wind meridional stress (Figure 11, 2nd panel), produces a positive meridional wind power input. The advective term cv_0 measures the net flux of MKE into the domain. This term is always negative, with minimum in winter and maximum in late spring and summer, when it approaches zero. The sign of this term is likely a result of the negative zonal gradient of MKE, as the mean AzC is weaker in the eastern part of the domain, with measured MKE values of *70* $cm^2\ s^{-2}$ at 32ºW decreasing to 28 $cm^2\ s^{-2}$ at 16ºW (Aguiar et al., 2011).

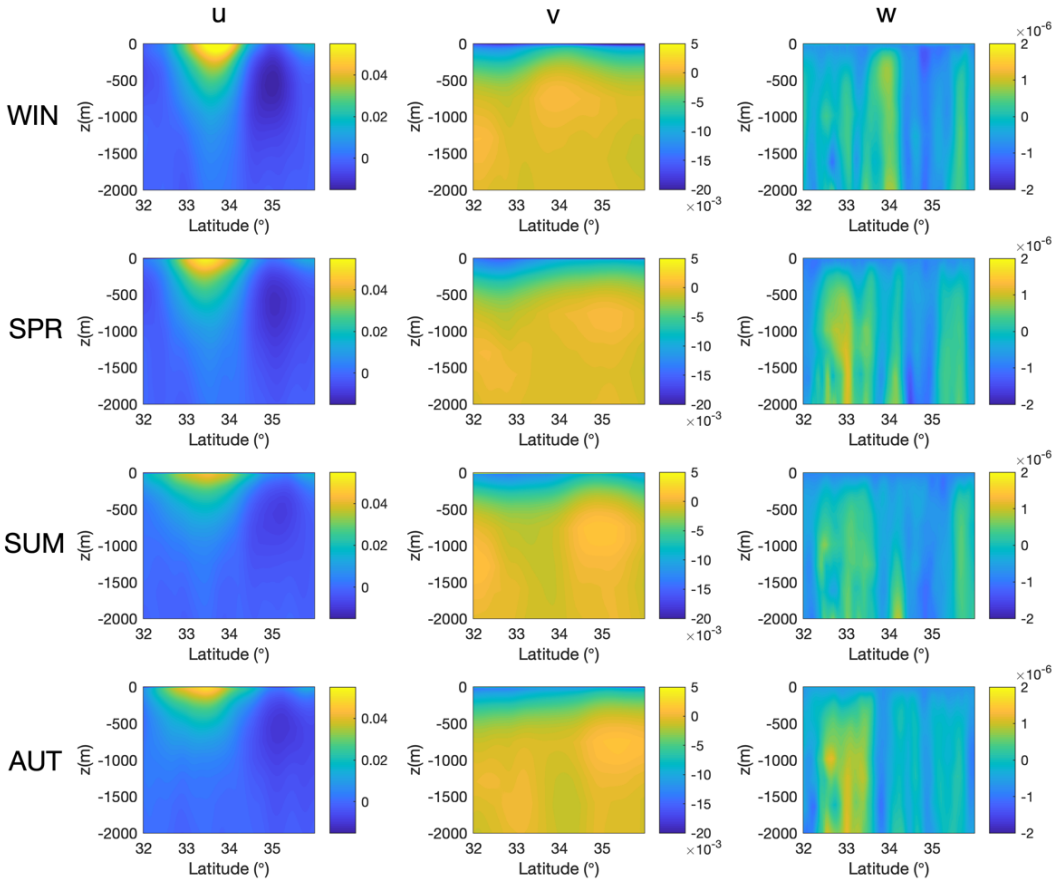

Figure 10. Seasonal average of mean velocity components in the AzC box. WIN: winter (DJF); SPR: spring (MAM); SUM: summer (JJA); AUT: autumn (SON).

The MPE → MKE transfer term cm_0 is fairly constant throughout the year, only rising conspicuously in early winter, as the stratification starts to weaken, since $\bar{w}$ does not show noticeable variations (Fig 8, right panels). The ck_0 term, which measures part of the barotropic transfer, is positive throughout the year with a local peak in mid-winter and then a slow rise during spring to a plateau in summer. This term isn't analyzed further since it is small compared to the other term in the barotropic energy transfer (*ck*).EKE terms are shown in Figure 12. The atmospheric forcing of EKE (*ca*) is negative for most of the year, exhibiting a positive phase during

winter, due to the increase in the zonal turbulent wind power input (Figure 11, 3rd panel). The meridional counterpart is one order of magnitude smaller (Figure 11, 4th panel). The advective flux term *cv* is largely positive but shows an important negative dip in mid-winter, followed by a sharp rise in late winter/early spring. This term involves averages of products of velocity components by EKE gradients. These are largely similar to MKE gradients (Aguiar et al., 2011): a negative zonal component and a meridional component that changes sign from positive southward to negative northward of the jet's core. Discarding the vertical, the negative phase of *cv* in the winter could be caused by the intensification of $\bar{u}$ in this season.

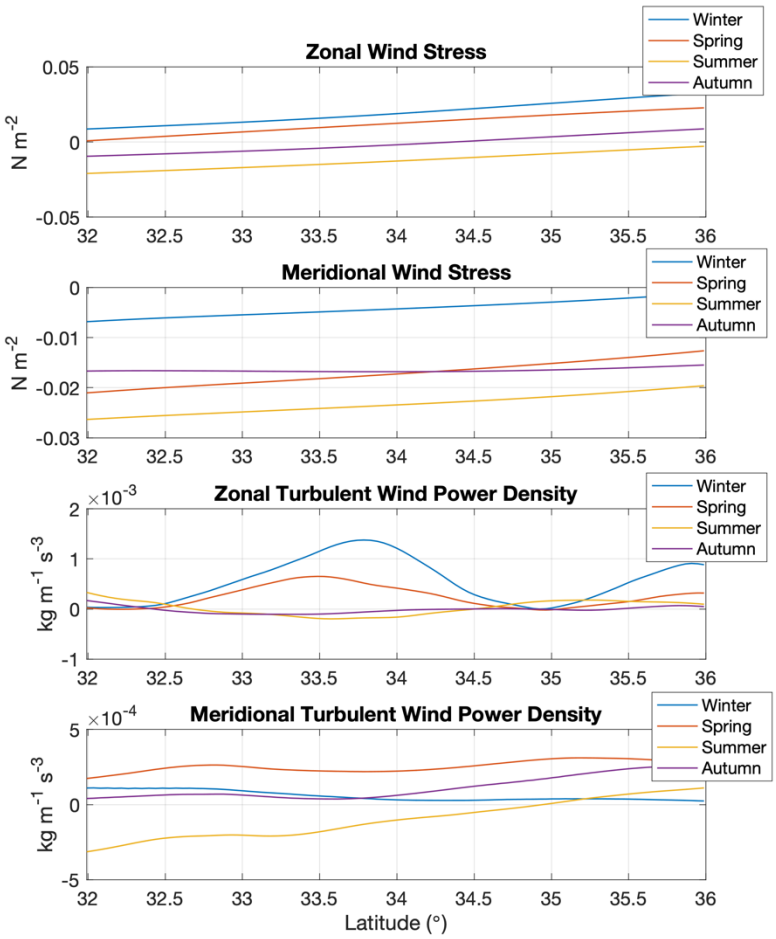

Figure 11. Seasonal variations of mean wind stress and turbulent wind power input in the AzC box.

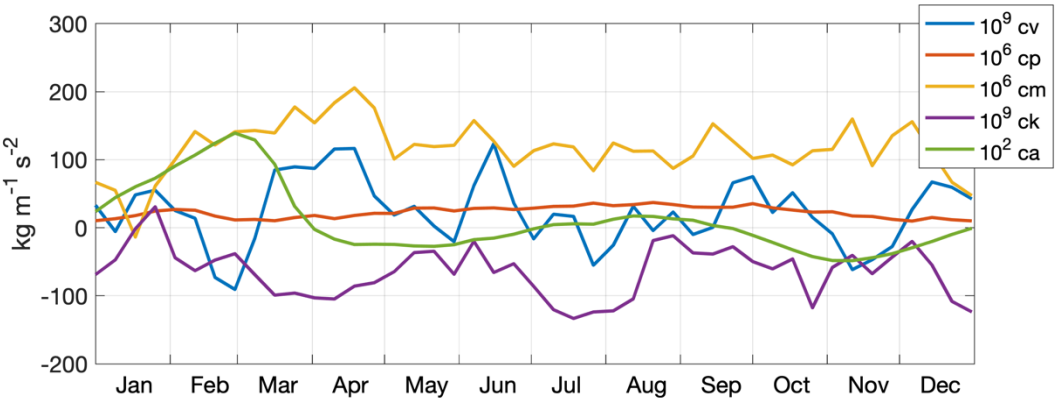

423

424 **Figure 12**. Annual cycle of volume averaged EKE density transfer terms. *Cv*: advective flux of MKE;
425 *cp*:turbulent pressure work; *cm*: Mean buoyancy work; *ck*: Reynolds stress (barotropic) work; *ca*:
426 wind stress work. Scaling applied as in Figure 9.

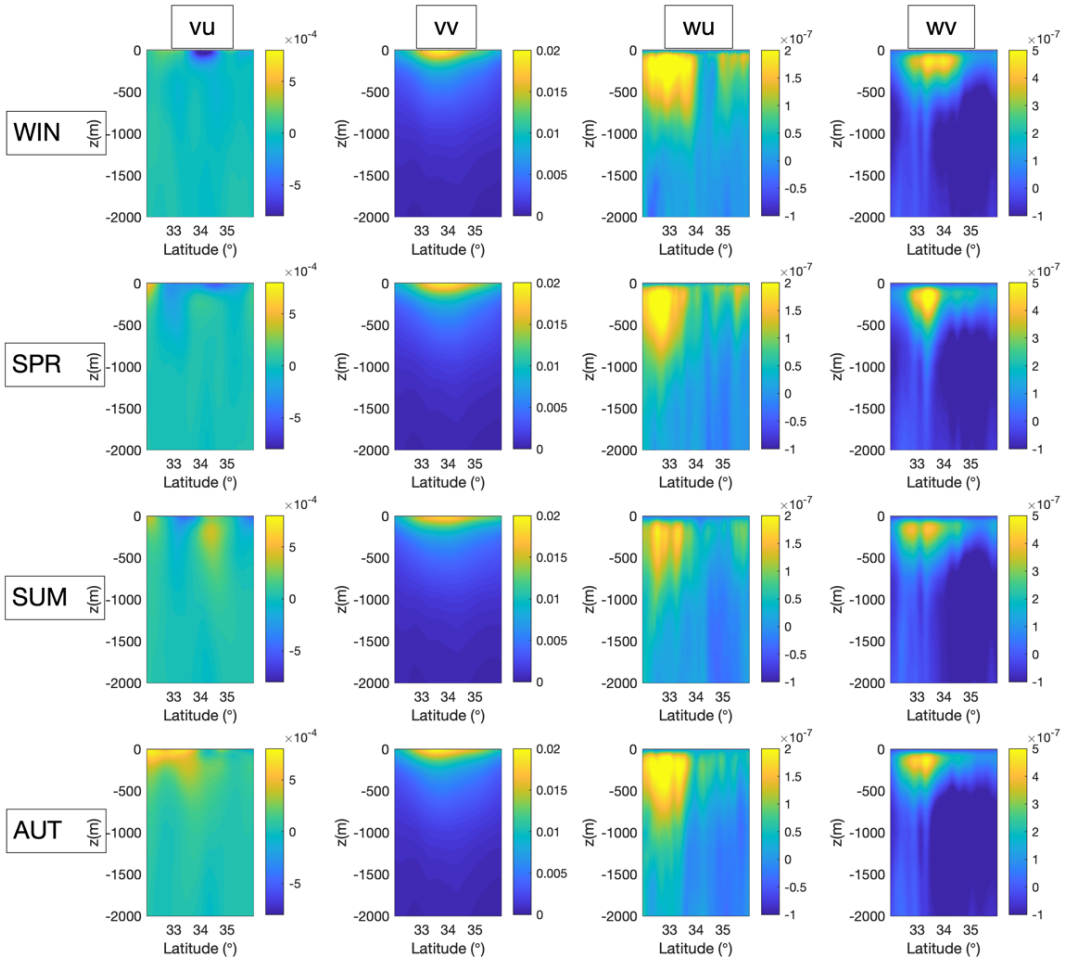

427

428 **Figure 13**. Seasonal maps of Reynolds stress terms. Season keys as in Figure 11.

429

The EPE→EKE transfer term *cm* is constant and positive along the year, which means that baroclinic instability is active throughout the year. The other component of the barotropic energy transfer (*ck*) is largely negative, adding to the reverse barotropic energy transfer that feeds MKE at the expense of EKE. The autocorrelation of the meridional velocity fluctuation $\overline{v'v'}$ is positive and concentrated just below the surface (Figure 13, 2nd column), where $\partial\bar{v}/\partial y$ is positive also (Figure 10, middle panels). The Reynolds stress $\overline{v'u'}$ is negative north of the AzC core, where $\partial\bar{u}/\partial y$ is also negative (Figure 10, left panels). Since these two are the dominant terms of *ck*, they explain the behavior of the seasonal evolution of the barotropic energy transfer term. The annual cycle of MPE density transfer terms (Figure 14) shows that advective fluxes of buoyancy (gv_0) are one order of magnitude smaller than MPE→EPE transfers (gp_0). The term shows an important increase (towards more negative values) in winter that, given that the main density gradients in the area are latitudinal, could be the result of the tilting of the axis of the mean AzC .

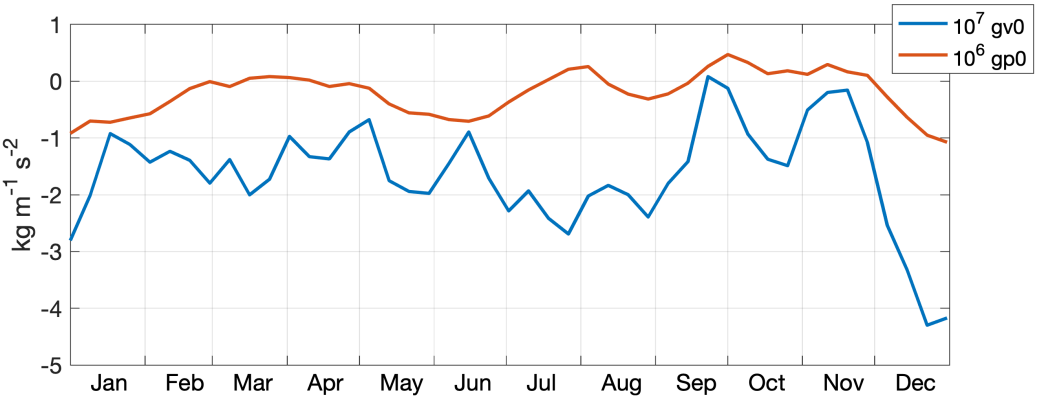

Figure 14. Annual cycle of volume averaged MAPE density transfer terms. gv_0: advective flux of MAPE; gp_0:MAPE to EAPE transfer. Scaling applied as in Figure 9.

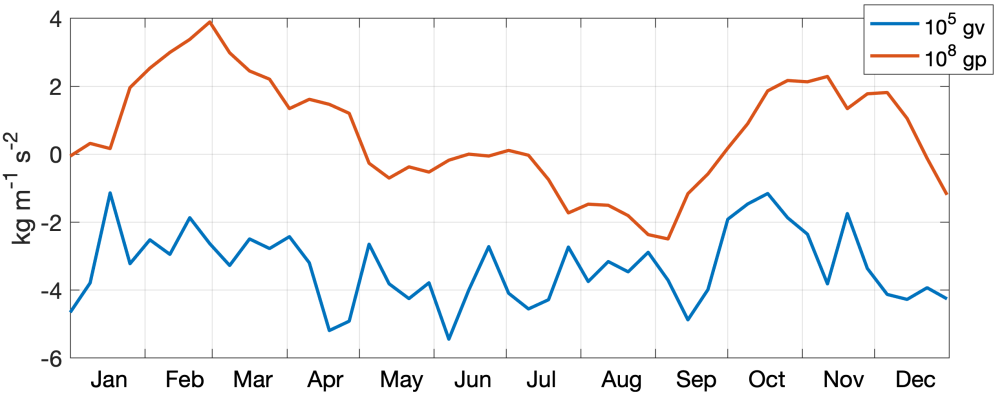

Figure 15. Annual cycle of volume averaged EAPE transfer terms. *gv*: advective flux of EAPE; *gp*:EAPE to MAPE transfer. All terms were scaled to fit the same range. Scaling applied as in Figure 9.

The EAPE density transfer terms *gv* and *gp* are shown in Figure 15. The EAPE → MAPE transfer *gp* is positive in later winter and spring and becomes negative afterward in summer, to rise to positive levels afterwards. If it is assumed that $\nabla\overline{\rho_a}$ is positive due to the upsloping of isopycnals at the edge of the subtropical gyre, then the dip in *gp*, that is $\propto -\overrightarrow{\overline{U'\rho'}_a} \cdot \nabla\overline{\rho_a}$, in the summer must

be due to positive correlations between fluctuating density anomalies and fluctuating velocities. The other term in the EAPE cycle is the advective flux of fluctuating density, *gv,* that is always negative and three orders of magnitude larger than *gp*, indicating that the mesoscale circulation is the dominant source of buoyancy flux, drawing buoyancy out of the AzC region throughout the year.

4 Discussion and conclusions

Although the AzC is stable throughout the year, seasonal variations in the quantities involved in its energetics are found. The main energy reservoir is the mean available potential energy, that is considerably larger than all the others. Energy from this reservoir is transformed in eddy kinetic energy by baroclinic instability, that is then transferred to mean kinetic energy by inverse barotropic energy transfer. This flow of energy occurs throughout the year and is well known from earlier studies of the energetics of baroclinically unstable ocean currents.

In spite of these internal dynamics, for MKE the dominant factor explaining its seasonality is atmospheric forcing (*ca0*; Figure 9) by several orders of magnitude. For EKE, atmospheric forcing (*ca*; Figure 12) also appears as the dominant factor and further investigation of the atmoshperic influence on the dynamics of the AzC is needed to clarify its role. For MAPE and EAPE the dominant factors are, respectively, eddy to mean potential energy transfers (*gp0*; Figure 14) and the advective flux of EAPE (*gv*; Figure 15).

In the energetics formulation of Kang and Curchitser (2015), the APE expression is a linearized version of the full APE expression, and therefore it is valid only in the case of linear stratification. To understand the effect of this simplification in the energetics cycle of the AzC, selected terms of the energy reservoirs and transfers were computed using the formulation of Aiki et al. (2016), that considers the full PE expression (Table 1).

Table 1. *Comparison of potential energy reservoirs and transfer rates computed with the formulations of Kang & Curchitser (2015) and Aiki et al. (2016). Energy reservoirs in TJ*; *Energy transfer rates in MW.*

	Winter		Spring		Summer		Autumn	
	KC15	AI16	KC15	AI16	KC15	AI16	KC15	AI16
MAPE	183.74	849.37	183.82	849.29	183.40	849.02	183.29	849.01
EAPE	6.72	41.38	6.73	41.30	6.71	41.40	6.70	41.52
cm0	-29.29		-2.26		-24.02		2.86	
cm	10.34	-22.37	19.27	-53.24	14.55	-38.14	13.98	-29.48
gv0	-15167	370690	-6029	180020	-13288	288170	-3989	-13464
gv	-2040	384.38	-1860	44.521	-2162	40.012	-1746	54.189
gp0	-80.58	96.48	-17.6	85.95	-34.04	33.06	16.03	53.55
gp[a]	0.356		0.304		-1.763		1.624	

Note. [a]In the formulation of Aiki et al (2016) *gp* = *gp0*.

Regarding the potential energy reservoirs, both the mean and the eddy available PE of Aiki et al. (2016) are one order of magnitude larger than those of Kang and Curchitser (2015), while being both quite stable thoughout the year. The larger value of MAPE for Aiki et al (2016) comes from the inclusion of the term $g(\rho-\rho_r)z$, which has been argued to be a misrepresentation of the local exact value of APE (Kang & Fringer, 2010). This term is also responsible for the large difference in the value of *gv0* in both formulations. The EAPE reservoir is larger for Aiki et al (2016) becausee it relies on the actual stratification and not on the reference one as for Kang and Curchitser (2015). Indeed, Figure 8 shows that the actual stratification is weaker than the reference

one, resulting in a larger APE. The MAPE → MKE transfer term *cm0* is the same for both formulations, whereas the EAPE → MKE transfer term *cm* is higher for Aiki et al (2016) due to the use of the actual stratification anomaly and not the anomaly with respect to the reference stratification; however the seasonal variation is the same for both formulations. The EAPE advective flux is lower and of opposite sign for Aiki et al (2016). The reason for this difference is not completely clear but we note that this latter formulation considers also the vertical advection of EAPE. For the MAPE → EAPE exchange terms, Aiki et al (2016) *gp0* and *gp* are equal, while this is not so for Kang and Curchitser (2015), due to the presence of the cross APE term in their formulation. While further study of the effect of the different available formulations is certainly warranted, it is out of the scope of this paper but will be addressed in future work.

Baroclinic energy transfers is the main internal energy transfer mechanism supporting the AzC energetics and it is stronger in early Spring, at the end of the winter mixing phase. As an open ocean current, baroclinic energy transfers are several order of magnitude larger than inverse barotropic energy transfers that feed the mean flow. This latter mechanism is active all year due to the Reynolds stress convergence northward of the AzC core, that can be understood through the meridional radiation of Rossby waves (Thompson, 1971), with a up-gradient momentum flux that sharpens the jet.The mean flow was observed to transfer energy to the available potential energy reservoir in all seasons except the autumn, with emphasis in the winter and summer.

These results support and extend the notion that the AzC is stable on yearly time scales. However, there are indications that interannually, the AzC may experience larger fluctuations due to large scale atmospheric forcing (Volkov & Fu, 2011). In addition, the timing of the energy cycle's several phases still needs to be identified in multi-year simulations of the AzC, to understand how it responds to interannual forcing.

Acknowledgements

This study has been made in the project OBSERVA.FISH: Autonomous Observing Systems in Fishing Vessels for the Support of Marine Ecosystem Management, which has been funded under contract (PTDC/CTA-AMB/31141/2017) by the Portuguese Foundation for Science and Technology (Fundação para a Ciência e Tecnologia - FCT) and by EU FEDER POR-Lisboa2020 and POR-Algarve2020 programs. This work also contributes to the Strategic Research Plan of the Centre for Marine Technology and Ocean Engineering (CENTEC), which is financed by FCT under the contract UIDB/UIDP/00134/2020.

The reservoir and energy transfer rates data used in the study are available at PANGEA repository via https://issues.pangaea.de/browse/PDI-29386 with CC-BY: Creative Commons Attribution 4.0 International license.

References

Abraham, E. R., & Bowen, M. M. (2002). Chaotic stirring by a mesoscale surface-ocean flow. *Chaos: An Interdisciplinary Journal of Nonlinear Science*, *12*(2), 373–381. https://doi.org/10.1063/1.1481615

Aguiar, A. C. B., Peliz, A. J., Pires, A. C., & Cann, B. L. (2011). Zonal structure of the mean flow and eddies in the Azores Current system. *Journal of Geophysical Research: Oceans (1978–2012)*, *116*(C2). https://doi.org/10.1029/2010jc006538

527 Aiki, H., Zhai, X., Greatbatch, R.J. (2016). Energetics of the Global Ocean: the Role of
528 Mesoscale Eddies, in S. K. Behere & T. Yamagata (Eds.), *Indo-Pacific Climate Variability*
529 *and Predictability, World Scientific Series on Asia-Pacific Weather and Climate* (Vol. 7, pp.
530 109–134). World Scientific,. https://doi.org/10.1142/9789814696623_0004

531 Álvarez-Salgado, X. A., Figueiras, F. G., Pérez, F. F., Groom, S., Nogueira, E., Borges, A. V., et
532 al. (2003). The Portugal coastal counter current off NW Spain: new insights on its
533 biogeochemical variability. *Progress in Oceanography*, *56*(2), 281--321.
534 https://doi.org/10.1016/s0079-6611(03)00007-7

535 Alves, M., Gaillard, F., Sparrow, M., Knoll, M., & Giraud, S. (2002). Circulation patterns and
536 transport of the Azores Front-Current system. *Deep Sea Research Part II: Topical Studies in*
537 *Oceanography*, *49*(19), 3983–4002. https://doi.org/10.1016/s0967-0645(02)00138-8

538 Alves, M. L. G. R., & Verdière, A. C. de. (1999). Instability Dynamics of a Subtropical Jet and
539 Applications to the Azores Front Current System: Eddy-Driven Mean Flow. *Journal of*
540 *Physical Oceanography*, *29*(5), 837–864. https://doi.org/10.1175/1520-
541 0485(1999)029<0837:idoasj>2.0.co;2

542 Beckmann, A., Böning, C. W., Brügge, B., & Stammer, D. (1994). On the generation and role of
543 eddy variability in the central North Atlantic Ocean. *Journal of Geophysical Research:*
544 *Oceans*, *99*(C10), 20381–20391. https://doi.org/10.1029/94jc01654

545 Brügge, B. (1995). Near-surface mean circulation and kinetic energy in the central North
546 Atlantic from drifter data. *Journal of Geophysical Research*, *100*(C10), 20543.
547 https://doi.org/10.1029/95jc01501

548 Chapman, D. C. (1985). Numerical Treatment of Cross-Shelf Open Boundaries in a Barotropic
549 Coastal Ocean Model. *Journal of Physical Oceanography*, *15*(8), 1060–1075.
550 https://doi.org/10.1175/1520-0485(1985)015<1060:ntocso>2.0.co;2

551 Gould, W. J. (1985). Physical oceanography of the Azores front. *Progress in Oceanography*, *14*,
552 167–190. https://doi.org/10.1016/0079-6611(85)90010-2

553 Haidvogel, D. B., Arango, H., Budgell, W. P., Cornuelle, B. D., Curchitser, E., Lorenzo, E. D., et
554 al. (2008). Ocean forecasting in terrain-following coordinates: Formulation and skill
555 assessment of the Regional Ocean Modeling System. *Journal of Computational Physics*,
556 *227*(7), 3595--3624. https://doi.org/10.1016/j.jcp.2007.06.016

557 Haidvogel, Dale B, & Beckmann, A. (1999). Numerical Ocean Circulation Modeling. *Series on*
558 *Environmental Science and Management*, 283–286.
559 https://doi.org/10.1142/9781860943935_0008

560 Ikeda, M. (1981). Meanders and Detached Eddies of a Strong Eastward-Flowing Jet Using a
561 Two-Layer Quasi-Geostrophic Model. *Journal of Physical Oceanography*, *11*(4), 526–540.
562 https://doi.org/10.1175/1520-0485(1981)011<0526:madeoa>2.0.co;2

563 Jia, Y. (2000). Formation of an Azores Current Due to Mediterranean Overflow in a Modeling
564 Study of the North Atlantic. *Journal of Physical Oceanography*, *30*(9), 2342–2358.
565 https://doi.org/10.1175/1520-0485(2000)030<2342:foaacd>2.0.co;2

566 Kang, D., & Curchitser, E. N. (2015). Energetics of Eddy–Mean Flow Interactions in the Gulf
567 Stream Region. *Journal of Physical Oceanography*, *45*(4), 1103–1120.
568 https://doi.org/10.1175/jpo-d-14-0200.1

569 Kang, D., & Fringer, O. (2010). On the Calculation of Available Potential Energy in Internal
570 Wave Fields. *Journal of Physical Oceanography*, *40*(11), 2539–2545.
571 https://doi.org/10.1175/2010jpo4497.1

572 Käse, R. H., Zenk, W., Sanford, T. B., & Hiller, W. (1985). Currents, fronts and eddy fluxes in
573 the Canary Basin. *Progress in Oceanography*, *14*, 231–257. https://doi.org/10.1016/0079-
574 6611(85)90013-8

575 Kida, S., Price, J. F., & Yang, J. (2008). The Upper-Oceanic Response to Overflows: A
576 Mechanism for the Azores Current. *Journal of Physical Oceanography*, *38*(4), 880--895.
577 https://doi.org/10.1175/2007jpo3750.1

578 Kielmann, J., & Käse, R. H. (1987). Numerical Modeling of Meander and Eddy Formation in the
579 Azores Current Frontal Zone. *Journal of Physical Oceanography*, *17*(4), 529–541.
580 https://doi.org/10.1175/1520-0485(1987)017<0529:nmomae>2.0.co;2

581 Klein, B., & Siedler, G. (1989). On the origin of the Azores Current. *Journal of Geophysical*
582 *Research: Oceans*, *94*(C5), 6159–6168. https://doi.org/10.1029/jc094ic05p06159

583 Krauss, W., & Käse, R. H. (1984). Mean circulation and eddy kinetic energy in the eastern North
584 Atlantic. *Journal of Geophysical Research: Oceans*, *89*(C3), 3407--3415.
585 https://doi.org/10.1029/jc089ic03p03407

586 Large, W. G., McWilliams, J. C., & Doney, S. C. (1994). Oceanic vertical mixing: A review and
587 a model with a nonlocal boundary layer parameterization. *Reviews of Geophysics*, *32*(4), 363–
588 403. https://doi.org/10.1029/94rg01872

589 Laurindo, L. C., Mariano, A. J., & Lumpkin, R. (2017). An improved near-surface velocity
590 climatology for the global ocean from drifter observations. *Deep Sea Research Part I:*
591 *Oceanographic Research Papers*, *124*, 73–92. https://doi.org/10.1016/j.dsr.2017.04.009

592 Lorenz, E. N. (1955). Available Potential Energy and the Maintenance of the General
593 Circulation. *Tellus*, *7*(2), 157--167. https://doi.org/10.3402/tellusa.v7i2.8796

594 Maillard, C., & Käse, R. (1989). The near-surface flow in the subtropical gyre south of the
595 Azores. *Journal of Geophysical Research: Oceans*, *94*(C11), 16133–16140.
596 https://doi.org/10.1029/jc094ic11p16133

597 Marchesiello, P., McWilliams, J. C., & Shchepetkin, A. (2001). Open boundary conditions for
598 long-term integration of regional oceanic models. *Ocean Modelling*, *3*(1–2), 1–20.
599 https://doi.org/10.1016/s1463-5003(00)00013-5

600 Martins, C. S., Hamann, M., & Fiúza, A. F. G. (2002). Surface circulation in the eastern North
601 Atlantic, from drifters and altimetry. *Journal of Geophysical Research: Oceans (1978–2012)*,
602 *107*(C12), 10-1-10–22. https://doi.org/10.1029/2000jc000345

603 Orlanski, I., & Cox, M. D. (1972). Baroclinic instability in ocean currents. *Geophysical Fluid*
604 *Dynamics*, *4*(1), 297–332. https://doi.org/10.1080/03091927208236102

605 Özgökmen, T. M., Chassignet, E. P., & Rooth, C. G. H. (2001). On the connection between the
606 Mediterranean outflow and the Azores Current. *Journal of Physical Oceanography*, *31*(2),
607 461--480. https://doi.org/10.1175/1520-0485(2001)031<0461:otcbtm>2.0.co;2

608 Peliz, Á., Rosa, T. L., Santos, A. M. P., & Pissarra, J. L. (2002). Fronts, jets, and counter-flows
609 in the Western Iberian upwelling system. *Journal of Marine Systems*, *35*(1–2), 61–77.
610 https://doi.org/10.1016/s0924-7963(02)00076-3

611 Peliz, Á., Dubert, J., Santos, A. M. P., Oliveira, P. B., & Cann, B. L. (2005). Winter upper ocean
612 circulation in the Western Iberian Basin—Fronts, Eddies and Poleward Flows: an overview.
613 *Deep Sea Research Part I: Oceanographic Research Papers*, *52*(4), 621–646.
614 https://doi.org/10.1016/j.dsr.2004.11.005

615 Peliz, A., Dubert, J., Marchesiello, P., & Teles-Machado, A. (2007). Surface circulation in the
616 Gulf of Cadiz: Model and mean flow structure. *Journal of Geophysical Research: Oceans*,
617 *112*(C11). https://doi.org/10.1029/2007jc004159

618 Pingree, R. D., Garcia-Soto, C., & Sinha, B. (1999). Position and structure of the
619 Subtropical/Azores Front region from combined Lagrangian and remote sensing
620 (IR/altimeter/SeaWiFS) measurements. *Journal of the Marine Biological Association of the*
621 *United Kingdom*, *79*(5), 769–792. https://doi.org/10.1017/s002531549900096x

622 Reverdin, G., Niiler, P. P., & Valdimarsson, H. (2003). North Atlantic Ocean surface currents.
623 *Journal of Geophysical Research: Oceans (1978–2012)*, *108*(C1), 2-1-2–21.
624 https://doi.org/10.1029/2001jc001020

625 Richardson, P. L. (1983). Eddy kinetic energy in the north atlantic from surface drifters. *Journal*
626 *of Geophysical Research*, *88*(C7), 4355--4367. https://doi.org/10.1029/jc088ic07p04355

627 Rossby, T. (1987). On the energetics of the Gulf Stream at 73W. *Journal of Marine Research*,
628 *45*(1), 59–82. https://doi.org/10.1357/002224087788400918

629 Saenz, J. A., Tailleux, R., Butler, E. D., Hughes, G. O., & Oliver, K. I. C. (2015). Estimating
630 Lorenz's Reference State in an Ocean with a Nonlinear Equation of State for Seawater.

631 *Journal of Physical Oceanography*, *45*(5), 1242–1257. https://doi.org/10.1175/jpo-d-14-
632 0105.1

633 Shchepetkin, A. F., & McWilliams, J. C. (2003). A method for computing horizontal pressure-
634 gradient force in an oceanic model with a nonaligned vertical coordinate. *Journal of*
635 *Geophysical Research: Oceans*, *108*(C3). https://doi.org/10.1029/2001jc001047

636 Shchepetkin, A. F., & McWilliams, J. C. (2005). The regional oceanic modeling system
637 (ROMS): a split-explicit, free-surface, topography-following-coordinate oceanic model.
638 *Ocean Modelling*, *9*(4), 347--404. https://doi.org/10.1016/j.ocemod.2004.08.002

639 Stramma, L., & Müller, T. J. (1989). Some observations of the Azores Current and the North
640 Equatorial Current. *Journal of Geophysical Research: Oceans*, *94*(C3), 3181–3186.
641 https://doi.org/10.1029/jc094ic03p03181

642 Stramma, L., & Siedler, G. (1988). Seasonal changes in the North Atlantic subtropical gyre.
643 *Journal of Geophysical Research: Oceans*, *93*(C7), 8111--8118.
644 https://doi.org/10.1029/jc093ic07p08111

645 Traon, P.-Y. L., & Mey, P. D. (1994). The eddy field associated with the Azores Front east of the
646 Mid-Atlantic Ridge as observed by the Geosat altimeter. *Journal of Geophysical Research:*
647 *Oceans*, *99*(C5), 9907--9923. https://doi.org/10.1029/93jc03513

648 Volkov, D. L., & Fu, L. (2011). Interannual variability of the Azores Current strength and eddy
649 energy in relation to atmospheric forcing. *Journal of Geophysical Research: Oceans (1978–*
650 *2012)*, *116*(C11). https://doi.org/10.1029/2011jc007271

651 Volkov, D. L., & Fu, L.-L. (2010). On the Reasons for the Formation and Variability of the
652 Azores Current. *Journal of Physical Oceanography*, *40*(10), 2197–2220.
653 https://doi.org/10.1175/2010jpo4326.1

654 Wood, R. A. (1988). Unstable Waves on Oceanic Fronts: Large Amplitude Behavior and Mean
655 Flow Generation. *Journal of Physical Oceanography*, *18*(5), 775–787.
656 https://doi.org/10.1175/1520-0485(1988)018<0775:uwoofl>2.0.co;2

657 Woodruff, S. D., Diaz, H. F., Elms, J. D., & Worley, S. J. (1998). COADS Release 2 data and
658 metadata enhancements for improvements of marine surface flux fields. *Physics and*
659 *Chemistry of the Earth*, *23*(5–6), 517–526. https://doi.org/10.1016/s0079-1946(98)00064-0

660